Nuclear Instruments and Methods in Physics Research A301 (1991) 202–214
North-Holland

Experimental determination of ionization cluster size distributions in counting gases

Hansjörg Fischle [1], Joachim Heintze and Bernhard Schmidt
Physikalisches Institut der Universität Heidelberg Philosophenweg 12, D-6900 Heidelberg, Germany

Received 15 October 1990

The distribution of the number of electrons contained in the ionization clusters formed along the track of minimum ionizing particles has been determined experimentally. Results are presented for argon, helium, methane, ethane, propane, isobutane and carbon dioxide, i.e., for gases which are commonly used as counting gases in drift chambers. The probabilities $w(n)$ for the formation of a cluster containing n electrons were found to be monotonically decreasing for increasing n. Typical values for $w(1)$ are 0.66 (Ar), 0.77 (He), and 0.79 (CH_4). The results are compared with model predictions.

1. Introduction

The wide-spread use of drift chambers in high energy physics experiments and in other applications is mainly motivated by the good space resolution and the large area of these detectors. The space resolution depends on a number of factors; one of them is the microscopic structure of the particle tracks. The "granularity" of the track, in combination with the drift time dispersion, can even be the dominating effect.

It is well known that the ionization along a particle track is not deposited as randomly distributed single electron–ion pairs but in lumps, or "ionization clusters", each cluster being produced as a result of an individual primary ionization act: The electron struck by the incident particle may acquire sufficient energy to ionize one or more additional atoms. Also more than one electron electron may be ejected from a single atom, e.g. by the Auger effect following inner-shell ionization.

The number of electrons per cluster, in the following referred to as "cluster size", may vary from $n = 1, 2, 3, \cdots$ up to very large values. In the latter case, it is more approximate to speak of δ-rays, since the cluster evolves into a visible track. At any rate, the cluster size is a function of the energy E transferred in the primary ionization act, n being roughly proportional to E. For large energy transfers (collisions with small impact parameter), the atomic binding of the struck electron can be neglected and the cross section is essentially given by the Rutherford scattering formula [1]:

$$\frac{d\sigma}{dE} = 0.255 \times 10^{-24}\ \text{cm}^2\ \text{MeV}\ \frac{z^2}{\beta^2 E^2}. \qquad (1)$$

z and β are the charge and velocity of the incident particle, respectively. For distant collisions the interaction with the whole atom has to be considered, which is difficult to calculate. This difficulty concerns the vast majority of ionizing collisions since distant collisions are by far more frequent than close collisions.

Very little is known experimentally about the cluster size distribution, i.e., about the probability $w(n)$ to produce in a primary ionization act a cluster containing n electrons. Early measurements with cloud chambers are the only piece of information [2,3]. A theoretical study of the cluster size distribution along the tracks of fast particles passing through argon was made by Lapique and Piuz [4]. These authors start from a formula for $d\sigma/dE$ given by Chechin et al. [5] covering the range of both small and large energy transfers. They determine the kinetic energies of the electrons ejected at a given value of E and study carefully the number of free electrons eventually released. The primary aim of the paper is to study the method of cluster counting [6] as a means of particle identification. However, the cluster size distribution obtained by Lapique and Piuz is generally used for simulation studies of the response of drift chambers, since it is so far the only source of information for numerical values of $w(n)$.

In the present paper, we report on an experimental determination of the cluster size distribution along the tracks of fast electrons ($\beta \approx 0.8$–0.97) in argon, helium and in some molecular gases which are commonly used

[1] Now at Siemens Matsushita, D7920 Heidenheim, Germany.

0168-9002/91/$03.50

in drift chambers. The method covers the range of one to about 15 electrons per cluster. It will be shown that beyond this range the cluster size distribution is essentially given by the Rutherford scattering approximation, eq. (1). Therefore, we will present the complete information on $w(n)$ for the gases mentioned above [#1].

2. Experimental method

In order to determine the number of electrons in ionization clusters, we first isolate an individual cluster, we then separate the electrons from each other and finally count the number of electrons. The apparatus is shown in fig. 1.

A ^{90}Sr source S is mounted in a collimator defining a narrow beam of β-rays. The β-particles cross two Geiger–Müller counters GM, the cluster extraction device CED, and a narrow opening in the scintillator SC2. They are finally stopped in the scintillator SC1, where their energy can be measured. The coincidence

$$((\mathrm{GM1\ or\ GM2}), \mathrm{SC1}, \overline{\mathrm{SC2}}) \qquad (2)$$

is used as a trigger signal indicating the passage of an electron through CED. If an ionization cluster is formed in the active part of the CED, the electrons are injected into a drift region, 42 cm long, in which they are separated from each other by diffusion. Finally, the electrons are counted at the counting wire CW. All elements of the apparatus are enclosed in a vessel filled with the gas under investigation.

2.1. Isolation of individual ionization clusters

The cluster extraction device CED is shown in fig 2. It consists of a central wire ($r_1 = 10$ μm) and two concentric tubes, the inner one with radius $r_2 = 2$ mm, the outer one with radius $r_3 = 20$ mm. These electrodes are connected to potentials HV1 and HV2 generating a radial electrical field. The inner tube carries a narrow slit (1 mm wide) defining the active part of the CED. The outer tube has a larger opening (15 × 15 mm^2). The β-particles pass the device as shown in fig. 2. Once a primary ionization cluster is formed in the active region, the electrons of the cluster are extracted. Due to the relatively high electric field at $r < r_2$, the initial diffusive displacement of the electrons is small (typically a few μm). The opening at r_3 is large enough so that all electrons are transferred into the drift space. HV1 and HV2 are adjusted such that the field at r_3 is equal to the homogeneous field in the drift space. The field at r_2 is about 10 times larger.

[#1] A more detailed description of this work is given in H. Fischle, Thesis (1990), Fakultät für Physik und Astronomie, Universität Heidelberg, Germany.

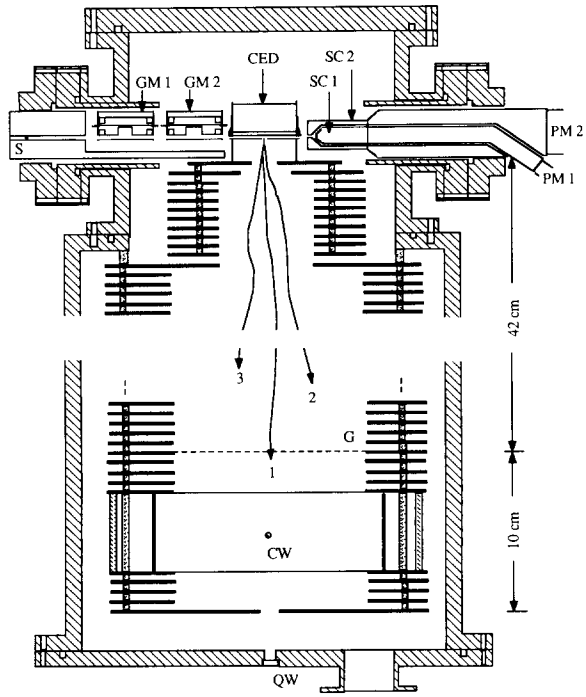

Fig. 1. Experimental apparatus. S: ^{90}Sr source, GM: Geiger counter, CED: cluster extraction device, SC: scintillators, G: grid, CW: counting wire, QW: quartz window.

We operate the device at gas pressures in the range of 100 Torr. At this pressure, we expect to produce an electron cluster in the active part of the CED with a probability of 10–20%, hence the probability to see more than one cluster at a time should be a few percent only.

2.2. Spatial separation of the electrons

At the formation, the spatial extension of a cluster is small, usually less than 100 μm. At the end of the drift space, the spatial distribution of the electrons is Gauss-

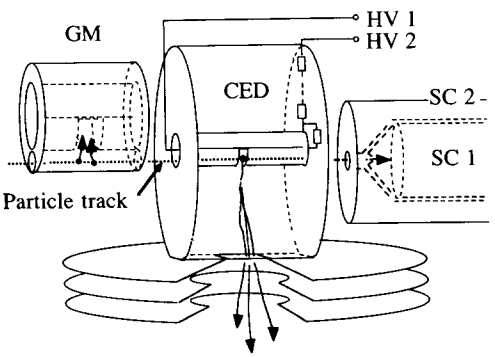

Fig. 2. Detailed view of the cluster extraction device.

ian with characteristic widths σ_l (longitudinal) and σ_t (transverse). The spread of the arrival times is given by σ_l and the drift velocity v_D. It should be considerably larger than the minimum resolvable arrival time difference which is given by the width of the counting pulse, typically 30 ns. For all gases investigated here, the drift parameters v_D, σ_l and σ_t and their dependence on the reduced field strength are known [7]. On this basis, the geometry of the drift space was fixed as shown in fig. 1. At an electrical field $E \approx 10$ V/cm, $p \approx 100$ Torr we expect a spread of the arrival times $\sigma_l/v_D \approx 1$ μs and a lateral spread of the electrons of the order of a few cm.

2.3. Detection of single electrons

For the work described here, it is most essential to detect the individual electrons with an efficiency close to 100% while operating the counting wire strictly in the proportional mode. The first feature is necessary in order to avoid tedious corrections which would seriously reduce the accuracy of the results. The second is essential for avoiding after pulses which would upset the correct electron counting. Separate studies were carried out in order to explore the operational conditions meeting these requirements.

For this purpose, cylindrical counting tubes equipped with quartz windows were operated at a gas pressure of 100 Torr. Single electrons were produced irradiating the tubes with UV light from a Hg lamp. Results obtained with different anode wire radii are shown in fig. 3. In the proportional regime, the pulse charge distribution is essentially given by an exponential function superimposed on a sharp drop at small pulse heights. We have to reach a gas amplification such that the drop occurs well above the amplifier noise level. Afterpulses are occurring if the gas amplification runs into a semi-Geiger mode. They are directly observable by oscilloscope; they manifest themselves in fig. 3 by deviations from the exponential slope [8]. We conclude that we can reach our goal by using rather thick counting wires: 400 μm wires for studying molecular gases such as CH_4, 800 μm wires for rare gas/CH_4 mixtures.

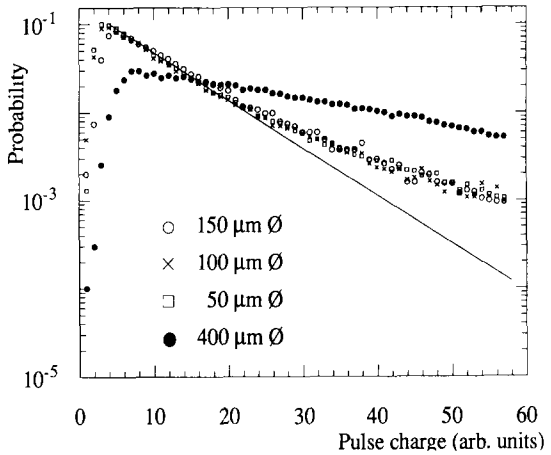

Fig. 3. Pulse charge spectra of single photoelectrons obtained in cylindrical counting tubes using different wire diameters. Gas filling: CH_4, 100 Torr. The full line is an exponential function fitted to the data points at low pulse charge.

The position of the counting wire is shown in fig. 1. A grid separates the drift space from the counting region. At the bottom of the gas vessel, a quartz window is mounted for the injection of UV light. By studying the pulse shape and the pulse charge distribution of single photoelectrons, it is possible to monitor the electron detection efficiency and the absence of afterpulses.

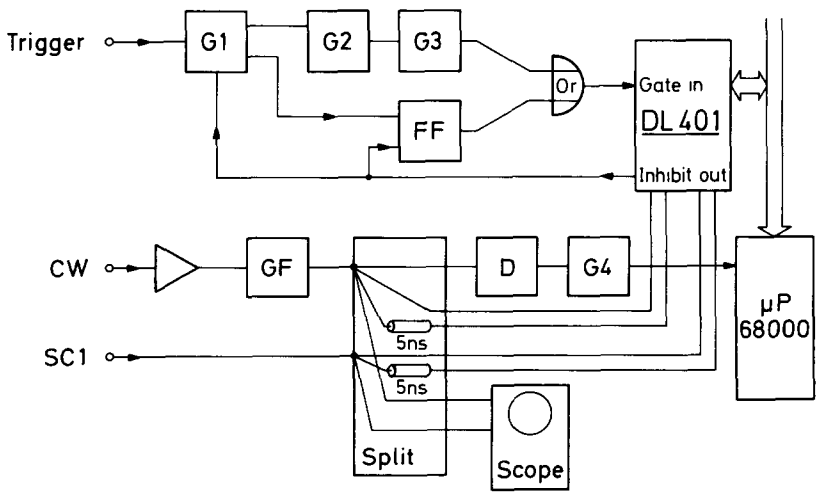

Fig. 4. Electronics. G1–G4: gate circuits, FF: flipflop, GF: Gauss filter, D: discriminator. DL401 is a Flash ADC module used as a waveform digitizer.

2.4. Electronics

The electronics used to record the signals of the counting wire CW is shown in fig. 4. A high-gain common-base amplifier with a FET source follower input stage followed by a Gaussian filter is connected to a passive split. At this stage, the rise time of the pulses is 10 ns and the rms noise level, counting wire connected, corresponds to the charge of 1850 electrons. As an example for the pulse shape obtained, we show in fig. 5 pulses from an ionization cluster containing three electrons.

Behind the split, the signals are fed into a 100 MHz FADC (DL401 [9]) both directly and through an additional delay of 5 ns. In this way the pulse shape is sampled with 200 MHz. The analog signal of the scintillation counter SC1 is digitized in a similar way. The signal from CW is also fed into a monitoring oscilloscope and, via a discriminator and gate G4, into a Motorola 68000 processor for enabling the readout of the FADC memories. The discriminator defines a hardware threshold for the detection of single electrons. This is done in order to avoid dead time by unnecessary readout processes. If after a trigger no read-enable is produced, an "empty trigger" is counted.

The FADCs are running continuously. They are stopped, through the action of G1 and the flipflop FF, by the trigger signal defined in section 2.1. The scintillator signal from SC1 is digitized and stored 200 ns before the stop. Then, after a time set by gate G2, the FADCs are started again, running for a time interval of 9.5 μs, which is set by gate G3. During this time, the electrons arriving at the counting wire are recorded. The time delay given by G2 is adjusted such that the average drift time falls approximately into the center of the 9.5 μs time interval.

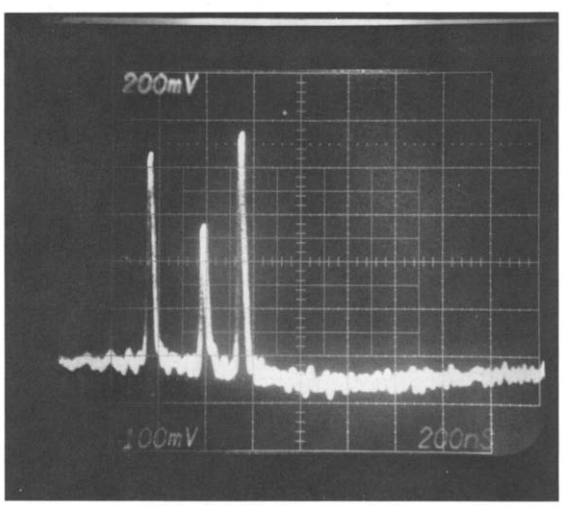

Fig. 5. Cluster containing three electrons. Event recorded with the monitoring oscilloscope. Horizontal scale: 200 ns per division.

2.5. Data taking and data processing

After a trigger followed by a readout enable signal, the memories of the FADCs are read by the 68000 processor as soon as the gate pulse from G3 stops. In order to detect electrons, a software threshold is defined as follows: The signal has to exceed, for at least four successive time bins, i.e. for at least 20 ns, a level of 3 times the rms noise level. The number of electrons in each event is determined by the number of signals recorded above the software threshold and by the number of "local maxima" within each signal. A local maximum is defined by three increasing charge samples followed by three decreasing samples. Using the UV lamp, it was made sure that double counting of single electrons is negligible with these criteria. On the other hand, an efficiency very close to 100% can be reached as we will show later.

For each electron, the timing and the amplitude of the pulse maximum is determined on line. However, also the complete FADC content is stored, so that off line a more detailed data analysis including a "hand scan" of selected events is possible.

A real-time program calculates cluster size distributions, time distributions and pulse height spectra. Furthermore, it provides, in a test mode, pulse height distributions of background, noise and single electrons from UV photons.

3. Measurements

3.1. Tests of the method

In order to ensure a good performance of the apparatus, the different components of the instrument were individually adjusted and tested.

3.1.1. The trigger

Fig. 6a shows the spectrum of SC1 (SC2 in anticoincidence) recorded with the ^{90}Sr β-source and with ^{137}Cs and ^{60}Co γ-sources. The latter two sources were used for calibration of the energy scale. In fig. 6b the pulse height distribution of SC1 is shown for particles fulfilling the trigger condition eq. (2). Requiring a GM counter in coincidence, the background from bremsstrahlung and from PM noise is eliminated. In comparison to the ^{90}Sr β-spectrum, the maximum of the spectrum shown in fig. 6b is shifted towards higher energies. This is due to losses of low-energy electrons by multiple scattering in the gas between the source and SC1. Fig. 6 shows that the signals of SC1 can be used to determine the energy of the triggering β-particles.

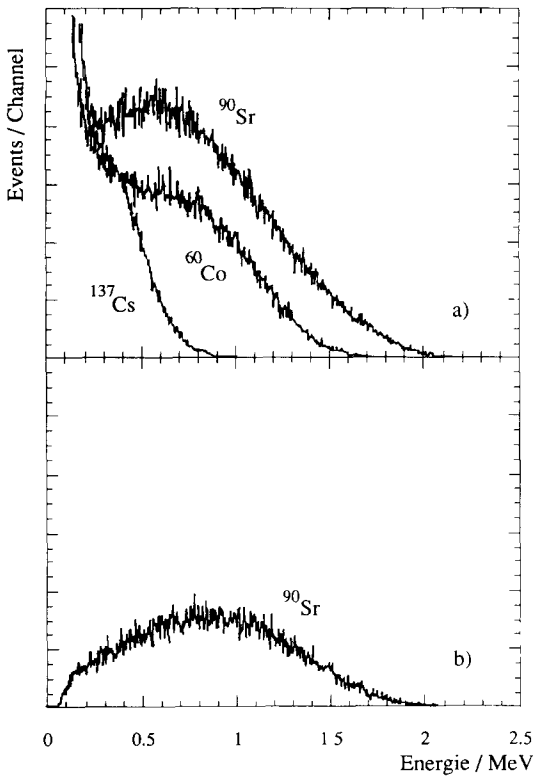

Fig. 6. Pulse height distributions of scintillator SC1. Spectra without coincidence requirement (a) and spectrum with GM in coincidence (b).

3.1.2. Electron drift and diffusion

Varying the electrical field in the drift region at a given pressure of the gas under investigation, the drift velocity was measured as a function of E/p. Good agreement with published data [7] was found. To check the transverse diffusion, two additional counting wires were mounted temporarily left and right of CW (fig. 1). It was found that no electrons are leaking out in lateral direction. The observed diffusion coefficients are consistent with data from ref. [7]. The longitudinal diffusion causes the time spread of the electrons. Fig. 7 shows the drift-time distributions observed in CH_4 and in Ar/CH_4 (9 : 1). It is seen that losses due to the 9.5 μs time window set by G2 are negligible. The widths of the curves are about 30% larger than expected from longitudinal diffusion alone. This is attributed to the drift-time dispersion along the path between grid and counting wire.

3.1.3. Electron attachment

In order to keep losses due to attachment of electrons to impurities of the gas at a low level, the apparatus was constructed of metal and ceramics, and highly purified gases were used for measurement. The losses vary with the drift time t according to the law

$$N(t) = N(0)\, e^{-At}, \tag{3}$$

A being the attachment rate. In order to investigate possible losses, the ratio (number of events with electrons detected)/(total number of triggers) was measured as a function of t. This quantity is a good measure for attachment: As will be shown later, about 70% of all clusters contain only a single electron. The drift time was varied by changing the electrical field in the drift space. We conclude that the loss is $\lesssim 1\%$. The reduced pressure used in this experiment helps to suppress electron attachment, since usually the coefficient A in eq. (3) is proportional to the gas pressure [10].

3.1.4. Resolving time

The shape of the single electron pulses and the algorithm used for electron counting defines a lower limit for the time interval in which two electrons can be counted separately. This limit can be determined using the observed distribution of the time separation of two electrons within the same cluster (fig. 8). We conclude that the resolving time is about 40 ns.

3.1.5. Single electron detection efficiency

This quantity is determined by injecting UV light at the bottom of the vessel, as explained in section 2.1.

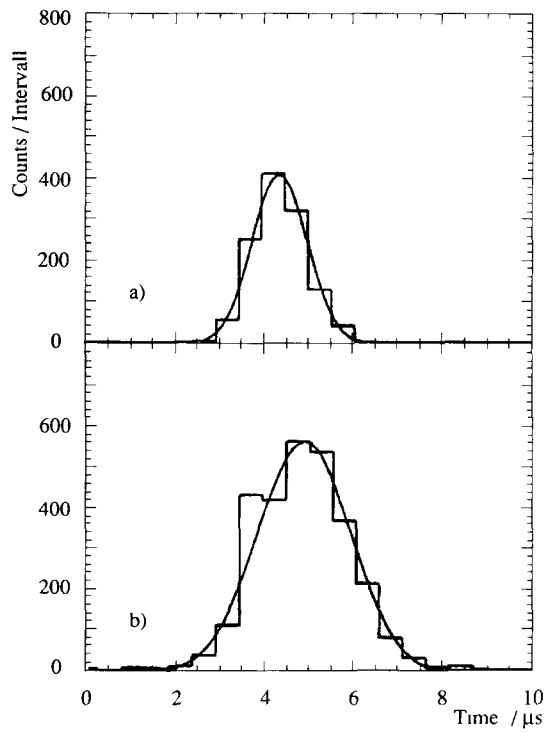

Fig. 7. Arrival time distributions, time scale with respect to the start of gate G3. (a) CH_4, (b) Ar/CH_4.

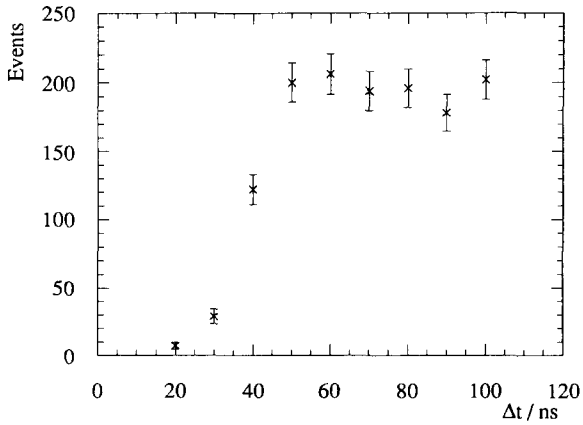

Fig. 8. Distribution of timing differences Δt of two successively recorded electrons.

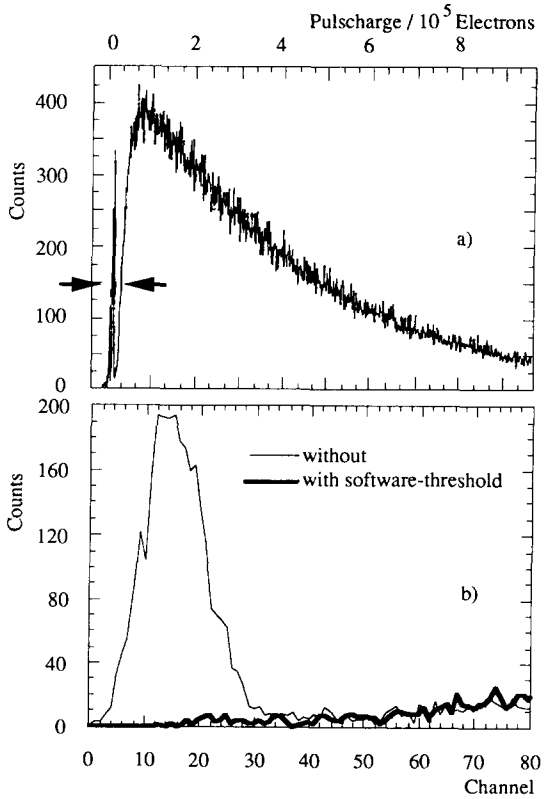

Fig. 9. (a) Pulse height distribution recorded with photoelectrons produced by injecting UV light through the quartz window shown in fig. 1. (b) shows, at an expanded scale, the lowest part of the spectrum, indicated by the arrows in (a).

Fig. 9a shows the charge spectrum of pulses passing the hardware threshold (section 2.4). Fig. 9b shows the lower part of this spectrum at an enlarged scale. Some noise pulses are passing the hardware threshold. Immediately above the noise level, the differential rate is close to zero and rises steeply for bigger pulse charges. It is seen in fig. 9b that the software threshold (section 2.5) suppresses the noise completely without affecting the remainder of the spectrum. We conclude that the single electron detection efficiency is very close to 100%.

3.2. Measurements of cluster size distributions

In table 1, the gases and gas mixtures used for measurements are specified. The pressures were chosen in order to maintain the primary ionization density as well as the single electron detection efficiency at the desired level. In CO_2, an admixture of CH_4 was necessary in order to meet the geometrical and timing requirements of the apparatus.

Data were taken in runs of about 24 hours, preceded and followed by measurements for adjustment and control of the apparatus. For each gas, the number of events recorded is listed in rows 4–6 of table 1. Beyond a certain cluster size n_{max}, which is given in the bottom row of table 1, the data are accumulated in the overflow bin. The definition of n_{max} was adjusted corresponding to the width of the arrival time distribution. All events in the overflow bin were scanned by hand (cf. section 2.5) in order to eliminate background arising from cosmic rays passing through the drift space in coincidence with real events of low electron multiplicity.

Table 1
Parameters of the gases used for measurement. Events (a) refers to the total number of triggers, (b) is the number of events with electrons recorded, (c) is the number of events in the overflow ($n > n_{max}$).

	CH_4(1)	CH_4(2)	Ar/CH_4	He/CH_4	CO_2/CH_4	C_2H_6	C_3H_8	i-C_4H_{10}
Pressure [Torr]	100	65	180	275	100	100	100	65
Mixing ratio			9:1	9:1	1:1			
Purity (%)	99.9995	99.9995	99.996	99.999	99.995	99.95	99.95	99.95
Events (a)	126166	60000	52000	24000	20183	6000	6000	4000
Events (b)	14340	5279	7633	2350	2264	1485	1710	1094
Events (c)	54	26	29	15	5	3	4	5
n_{max}	15	15	18	17	17	15	15	15

There was no problem to identify such events. The raw data, i.e. the number of events observed at cluster size n and in the overflow bin, are subject to corrections which will be discussed in the next section.

4. Data evaluation and results

4.1. Correction of the raw data

4.1.1. Electron losses

The probability that an electron, after leaving the CED, produces a pulse above the software threshold is called the electron detection efficiency ϵ. Contributions to the inefficiency $(1-\epsilon)$ could come from insufficient gas amplification, from electron attachment and from losses by diffusion. All of them are estimated to be small (section 3.1). Nevertheless, the influence of possible inefficiencies has to be discussed.

The true cluster size distribution $w(n)$ is related to the observed distribution $h(m)$ by the expression

$$h(m) = \sum_{n=m}^{\infty} \binom{n}{m} \epsilon^m (1-\epsilon)^{n-m} w(n). \tag{4}$$

In order to evaluate the relation between h and w, we compute correction factors $c_1(n) = w(n)/h(n)$ by replacing in eq. (4) the unknown function $w(n)$ by model functions $w'(n) = \text{const}\, n^{-\delta}$. The slopes observed in the raw data lead us to the following choice:

$$\text{argon:} \qquad w'(n) = \text{const}\, n^{-2}, \tag{5}$$

$$\text{methane:} \qquad w'(n) = \text{const}\, n^{-2.6}, \quad (n = 1, \ldots, 19),$$
$$= \text{const}\, n^{-2}, \quad (n \geq 20). \tag{6}$$

The constants were determined requiring $\Sigma w'(n) = 1$. In both cases, we assumed for large n an exponent $\delta = 2$. This assumption will be discussed in section 4.3. For carbon dioxide, the correction factors for argon were used. For helium and for the hydrocarbons we used those of methane.

Fig. 10a shows $c_1(n)$ for $\epsilon = 0.98$ and for $\epsilon = 0.95$. The corrections are smaller than the statistical errors of the data points $h(n)$. From the measurements described in section 3.1 we deduced $\epsilon \gtrsim 0.98$. Therefore, no correction for electron losses is made.

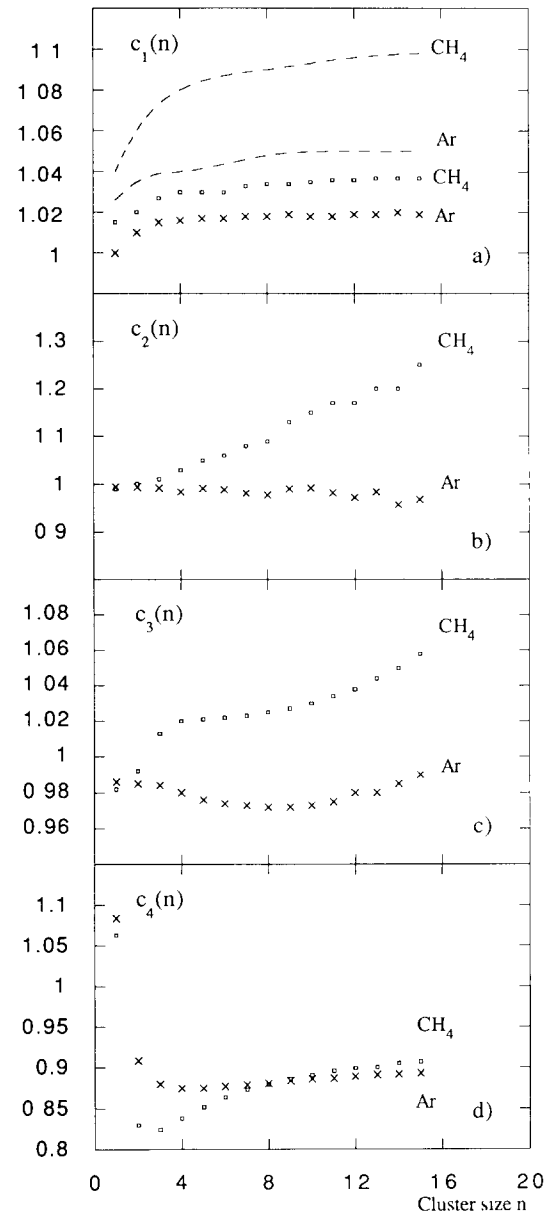

Fig. 10. Correction factors $c_i(n)$. (a) Efficiency correction. Points: $\epsilon = 0.98$, dashed lines. $\epsilon = 0.95$ assumed. (b) Correction for overlapping pulses. (c) Edge-effect correction (d) Correction for multiple cluster formation.

4.1.2. Resolving time

The resolving time for counting two electrons separately produces a deficit in electron counting depending on the cluster size and on the ratio α of the resolving time to the rms time spread of the arrival time distribution. The first is given by the Δt distribution, fig. 8, the second by distributions of the type shown in fig. 7. The numerical values were in the range of $\alpha = 0.03$ (He/CH_4) and $\alpha = 0.06$ (CH_4). In order to account for this effect, correction factors $c_2(n)$ were calculated. The relation between the observed distribution $h(m)$ and the true cluster size distribution $w(n)$ is given by the expression

$$h(m) = \sum_{n=m}^{\infty} a_{mn} w(n). \tag{7}$$

The coefficients a_{mn} were determined by a Monte Carlo simulation assuming, in accordance with fig. 7, a Gauss-

ian time distribution for n electrons arriving. For the evaluation of $c_2(n) = w(n)/h(n)$ the model functions eqs. (5) and (6) were inserted in eq. (7). Results are shown in fig. 10b. The correction also affects the content of the overflow bin, since some events recorded in the range $n \gtrsim 12$ are shifted to the overflow. For practical reasons; the summation in eq. (7) was stopped at $n = 35$. This has no influence on the accuracy of $c_2(n)$.

4.1.3. Edge effects

The boundaries of the active part of the CED, determined by the width of the slit shown in fig. 2 and by the field configuration in this part of the apparatus, give rise to edge effects. Due to the range of the electrons produced in the primary ionization process, in some events only a fraction of the ionization cluster is transferred to the drift space. As a consequence, some events with large cluster size are observed as events with medium or small cluster sizes. In order to correct for this effect, we assume [#2] that the electrons forming an ionization cluster of size n are, on average, homogeneously distributed in a sphere with radius $R' \approx 0.5R(n)$, where R is the extrapolated projected range of electrons causing a cluster of size n. The detected part of the cluster is set equal to the fraction of this spherical volume falling into the active part of the CED. Both ionization acts inside and outside this region are taken into account.

The range of very low energy electrons ($E = 50$ eV–1 keV) has been determined experimentally by Cole [12]. From these data, $R(n)$ is deduced using the relation $n = E/W_0$, with W_0 the average energy required to produce an ion pair. For W_0 we used table values [13]. For the He/CH_4 mixture, we assumed $W_0 = 28$ eV taking into account the Jesse effect [14] which will be discussed in the next section. The effective length Δx of the active part of CED was determined by comparing the fraction of "empty triggers" with the primary ionization densities determined by Rieke and Prepejchal [15]. The results are in the range $\Delta x \approx 0.3, \ldots, 0.4$ mm, depending on the applied voltages. On this basis, matrix elements a_{mn}, to be inserted in eq. (7), were calculated. The correction factors $c_3(n)$ (fig. 10c) were determined in the way described above for $c_1(n)$ and $c_2(n)$. In this case, the summation in eq. (7) was stopped at $n = 66$, corresponding to $E \approx 1.5$ keV. These corrections applied, the data recorded with CH_4 at 100 and at 65 Torr are in mutual agreement.

[#2] This assumption can be justified by the observation that the scattering of a electrons of a few 100 eV is dominated by elastic and inelastic scattering on atoms and molecules. In contrast to Coulomb scattering on atomic nuclei, the atomic and molecular scattering in this energy range is more or less isotropic. The cross sections are of the order of a few times 10^{-16} cm^2 [11]

4.1.4. Multiple cluster formation

In spite of the low pressure used in this experiment, there is a fraction of events with $N > 1$ clusters generated in the active part of the CED. This modifies the expectation for the observed cluster size distribution $h(n)$ according to Poisson-probabilities $P(N, \bar{N})$:

$$\begin{aligned} h(1) &= P(1, \bar{N}) = w(1), \\ h(2) &= P(1, \bar{N})w(2) + P(2, \bar{N})[w(1)]^2, \\ h(3) &= P(1, \bar{N})w(3) + P(2, \bar{N})2w(1)w(2) \\ &\quad + P(3, \bar{N})[w(1)]^3, \\ h(4) &= \cdots. \end{aligned} \tag{8}$$

The mean value $\bar{N}$ is determined by the fraction of "empty trigger" events: $P(0, \bar{N}) = \exp(-\bar{N})$. Inserting into eq. (8) the model distribution functions given by eqs. (5) and (6), correction factors $c_4(n) = w(n)/h(n)$ are computed. The results are shown in fig. 10d.

4.2. Evaluation of gas mixtures

The results obtained with gas mixtures are analyzed assuming that the cluster size distribution $w_{12}(n)$ of a mixture of gases 1 and 2 is related to the distributions $w_1(n)$ and $w_2(n)$ by the simple relation

$$w_{12}(n) = \frac{\pi_1}{\pi_1 + \pi_2} w_1(n) + \frac{\pi_2}{\pi_1 + \pi_2} w_2(n). \tag{9}$$

π_1 and π_2 are the partial pressures of the components 1 and 2, multiplied by the specific primary ionization cross sections [15]. Eq. (9) does not take into account that secondary ionization in gas mixtures may involve physical process which are absent in the corresponding pure gases. Such processes are very pronounced in helium (Jesse effect). In presence of an admixture X, the reaction

$$He(2^1S) + X \rightarrow He(1^1S) + X^+ + e^- \tag{10}$$

takes place and modifies strongly the secondary ionization yield [14]. If the concentration of X exceeds a few times 10^{-4}, W_0 changes from 46 (pure He) to 28 eV, rather independently of the chemical nature and the concentration of X. This number was already used in the previous section. We conclude that eq. (9) can also be used for He/CH_4 keeping in mind that the result presented here for He will refer to "He with some admixture". This is fully adequate for the study of counting gases.

According to arguments given in ref. [4], a reaction of the type (10) is not expected to be important for Ar/CH_4 mixtures. Also in CO_2/CH_4 we do not expect strong deviations from eq. (9).

4.3. Results

Fig. 11a–d and table 2 show the results for methane, argon, helium, and CO_2, all corrections applied. The data for Ar, He and Co_2 have been evaluated using eq. (9). The full lines are eye-fits through the data. The dashed line is the proposed extrapolation of our data towards higher values of n. It was obtained as follows:

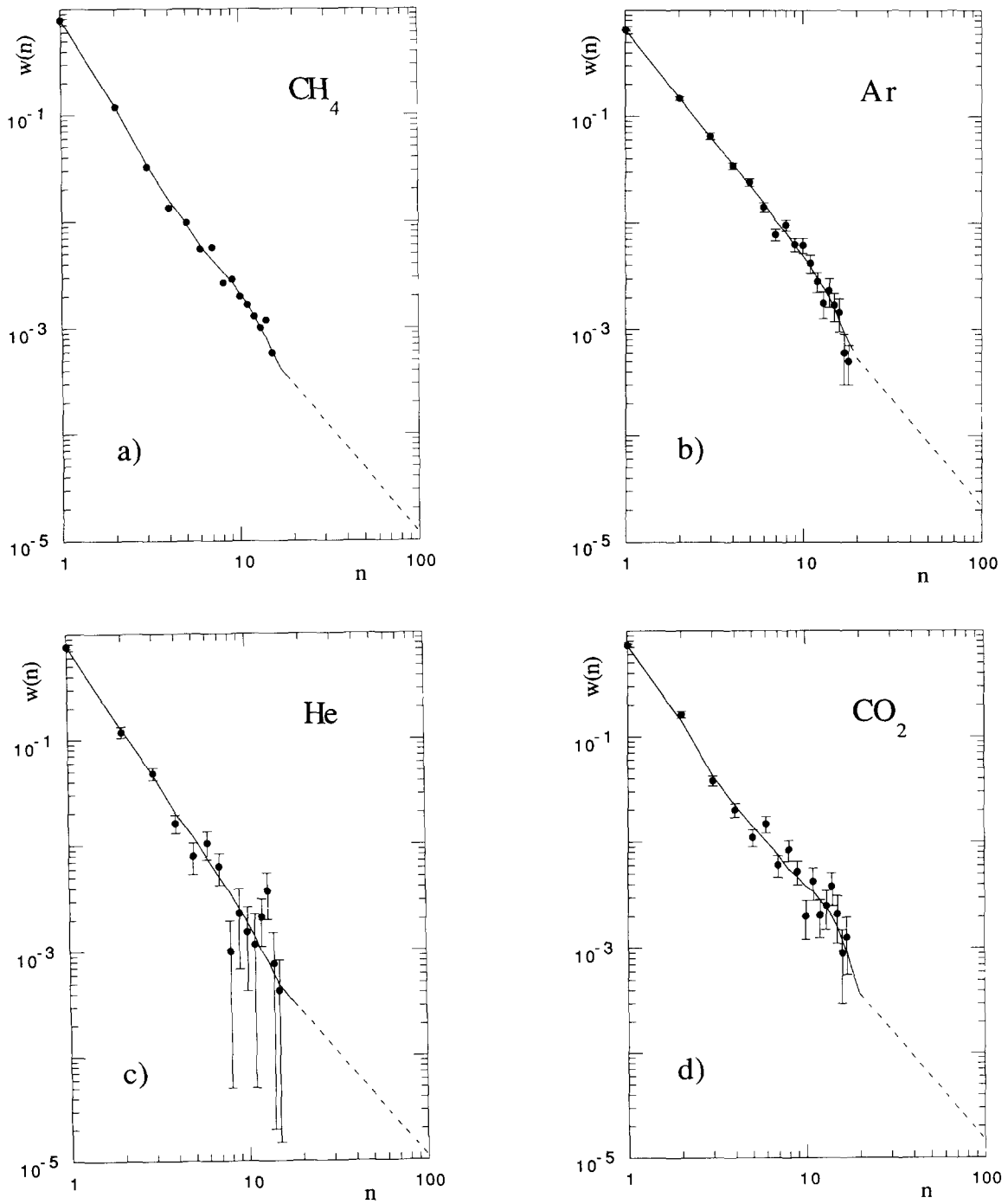

Fig. 11. Experimental results for cluster size distributions $w(n)$. Full line: eye-fit through the data points. Dashed line: Rutherford tail, prediction by the model described in section 4.3. The curve in (c) is identical to the curve in (a). The errors of the data points for C_2H_6 and for i-C_4H_{10} are similar to those of C_3H_8.

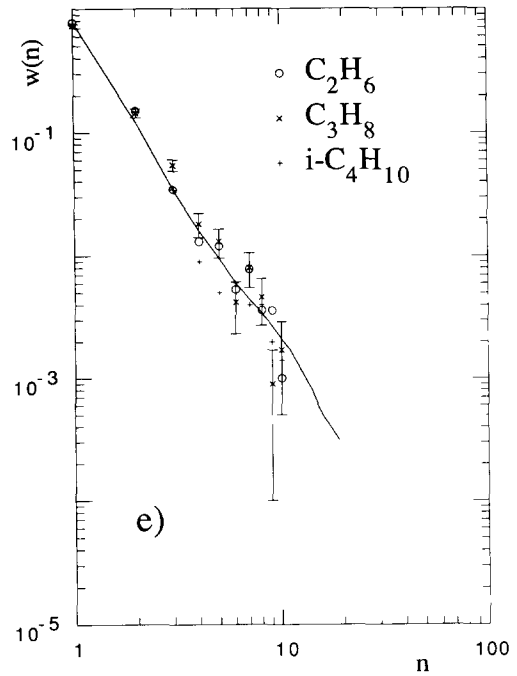

Fig. 11 (continued).

The fraction of events with energy transfers large enough to ionize n' electrons (and not more) is

$$q(n') = \frac{1}{\sigma_{tot}} \int_{n'I_0}^{(n'+1)I_0} \frac{d\sigma}{dE}\, dE. \qquad (11)$$

I_0 is the ionization potential of the atom (molecule), $d\sigma/dE$ the differential energy transfer cross section per atom (molecule) and σ_{tot} is the total primary ionization cross section. At a given n', we assume that ionization clusters are produced according to a binomial probability distribution. We then obtain the following expression for $w(n)$:

$$w(n) = \sum_{n'=n}^{\infty} q(n') \binom{n'}{n} p^n (1-p)^{n'-n}. \qquad (12)$$

The probability $p = \bar{n}/n'$ is set to $p = I_0/W_0$. In order to obtain a numerical prediction for $w(n \geq 20)$, we used for σ_{tot} the experimental values of Riecke and Prepejchal [15] and for $d\sigma/dE$ the Rutherford cross section, eq. (1), multiplied by the effective number of electrons per atom (molecule). All electrons are taken into account except the K-electrons of Ar whose binding energy ($E_k = 3.2$ keV) is far beyond our range of interest. The results are presented in the bottom row of table 2 and as the dashed lines in fig. 11a–d. The gap between n_{max} and $n = 20$ is closed by extending the eye fit. The extrapolation fits well our data points. Moreover, the observed overflow (corrections applied) agrees with the predicted overflow as shown in table 3. This can be considered as a justification of the assumptions made above.

In order to facilitate practical applications of our results, e.g. in the simulation of particle tracks, we include in table 2 numerical values corresponding to the full lines in fig. 11. In brackets, the proposed values for the extrapolation of our measurements are given.

Table 2
Cluster size distributions $w(n)$; (a) data points: (b) numerical values referring to the full lines in fig. 12. In brackets extrapolation of the data for $n > n_{max}$ according the the model described in section 4.3. All numbers in percent.

n	CH_4		Ar		He		CO_2	
	(a)	(b)	(a)	(b)	(a)	(b)	(a)	(b)
1	78.7 ±1.20	78.6	65.6 ±1.58	65.6	76.7 ±4.23	76.60	73.0 ±2.8	72.50
2	11.9 ±0.35	12.0	14.8 ±0.67	15.0	11.9 ±1.46	12.50	16.2 ±1.2	14.00
3	3.24±0.16	3.4	6.49±0.45	6.4	4.80±0.63	4.60	3.80±0.4	4.20
4	1.34±0.09	1.6	3.37±0.25	3.5	1.61±0.31	2.0	2.00±0.3	2.20
5	0.98±0.09	0.95	2.44±0.19	2.25	0.79±0.26	1.2	1.10±0.20	1.40
6	0.55±0.07	0.60	1.41±0.14	1.55	1.04±0.31	0.75	1.47±0.26	1.00
7	0.57±0.07	0.44	0.78±0.10	1.05	0.63±0.21	0.50	0.60±0.14	0.75
8	0.27±0.05	0.34	0.95±0.11	0.81	0.10±0.09	0.36	0.84±0.19	0.55
9	0.29±0.04	0.27	0.63±0.09	0.61	0.23±0.16	0.25	0.52±0.13	0.46
10	0.20±0.03	0.21	0.62±0.10	0.49	0.15±0.11	0.19	0.20±0.08	0.38
11	0.16±0.03	0.17	0.42±0.08	0.39	0.12±0.11	0.14	0.42±0.14	0.34
12	0.13±0.03	0.13	0.28±0.06	0.30	0.21±0.10	0.10	0.21±0.08	0.28
13	0.10±0.02	0.10	0.18±0.05	0.25	0.37±0.17	0.08	0.25±0.10	0.24
14	0.12±0.02	0.08	0.23±0.07	0.20	0.08±0.07	0.06	0.38±0.13	0.20
15	0.06±0.02	0.06	0.17±0.05	0.16	0.04±0.04	0.048	0.21±0.10	0.16
15		(0.050)	0.14±0.05	0.12	0.00±0.04	(0.043)	0.09±0.06	0.12
17		(0.042)	0.06±0.03	0.095	0.04±0.04	(0.038)	0.13±0.07	0.09
18		(0.037)	0.05±0.02	0.075		(0.034)		(0.064)
19		(0.033)		(0.063)		(0.030)		(0.048)
≥ 20		$(w(n) = 11.9/n^2)$		$(21.6/n^2)$		$(10.9/n^2)$		$(14.9/n^2)$

Table 3
Overflow data; measured overflow ($n > n_{max}$) from table 2, corrections applied, and predictions from the model described in section 4.3.

	CH_4	Ar	He	CO_2
Measured [%]	1.05 ± 0.14	1.06 ± 0.22	1.7 ± 0.7	0.6 ± 0.3
Predicted [%]	0.77	1.13	0 70	0.87

The results for ethane, propane, and isobutane are presented in fig. 11e. The full line is the same as in fig. 11a (methane). The data points show no significant deviations from the full line suggesting that the CH_4 data in table 2 can also be used for the other hydrocarbons.

In order to investigate a possible energy dependence of $w(n)$, the data samples of CH_4 and Ar/CH_4 were divided into two subsamples: One reaching from 0.75 MeV to 2 MeV and containing essentially minimum ionizing particles ($\beta \approx 0.95$), and one sample containing the data in the range of 250–750 keV ($\beta \approx 0.85$). No differences in $w(n)$ are observed.

5. Discussion and conclusions

The results obtained with the gases investigated here show that the cluster size distributions of very light elements contain a larger proportion of single electron clusters than those of more complex atoms. The effect is not very pronounced, $w(1)$ changing from 0.79 for methane to 0.66 for argon.

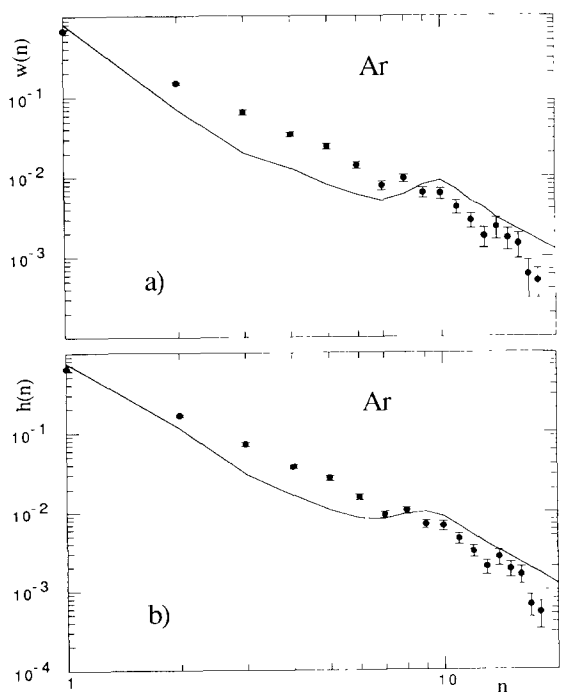

Fig. 12. (a) Comparison of the data for argon with the prediction of Lapique and Piuz [4], full line. (b) Comparison of the prediction [4], instrumental effects taken into account, with the raw data $h(n)$ recorded with Ar/CH_4 (9 : 1).

Earlier experimental investigations of $w(n)$ have been carried out by Wilson [2] and by Beekman [3] using a cloud chamber method. The results differed considerably from each other. Correcting Wilsons data for diffusive effects, the discrepancy could be removed [16]. Beekman obtained with 320 keV electrons in air $w(1) = 62\%$, $w(2) = 20\%$, $w(3) = 9\%$, $w(4) = 4\%$, $w(5) = 2\%$ and $w(n \geq 6) = 3\%$. These results are similar to those obtained for argon in the present work.

A comparison of the argon data with the calculations of Lapique and Piuz [4] is shown in fig. 12. Our data point for single electron clusters, $w(1) = 0.656 \pm 0.016$, is considerably lower than the predictions $w(1) = 0.802$ and 0.841, respectively, depending on the model. Moreover, our data do not reproduce a salient feature of that calculation, namely the pronounced bump in the distribution near $n = 10$. According to our estimates, the bump could not have been washed out in the data by instrumental effects. Inserting the distribution $w(n)$ obtained by Lapique and Piuz in eqs. (7) and (8) and using the same matrix elements a_{mn} as before, we obtain the line shown in fig. 12b. The bump should have been clearly visible in the raw data of this experiment.

The physical reason for the maximum in the theoretical curve is an increased probability for energy transfers above $E = 250$ eV, the $L_{II,III}$ absorption edge of argon. It is predicted that at this energy transfer preferentially an L electron is knocked out. Subsequently, the argon atom emits an Auger electron from the M shell with an energy $E_{kin} \approx 200$ eV capable to ionize about nine further atoms. The formula of Chechin et al. [5] which was used in ref. [4] predicts that the differential cross section $d\sigma/dE$ is essentially proportional to the distributed oscillator strength $f_c(E)$, which is in turn proportional to the photon absorption cross section:

$$f_c(E) = \sigma_\gamma(E)/1.097 \times 10^{-16} Z. \quad (13)$$

The absorption of a virtual photon of energy E is treated as the absorption of a real photon of the same energy. Consequently, the bump in fig. 12 reflects the well known L absorption edge of argon. We note that the underlying assumption connecting $d\sigma/dE$ and $f_c(E)$ is usually made in the theory of ionizing atomic collisions [17], specifically if numerical results are to be obtained [18]. Our data suggest that this treatment may not be appropriate for describing ionization by relativistic particles.

In the following, we consider an alternative model for the derivation of $w(n)$, not using the photon absorption cross section as an input. We start from measured spectra of electrons produced in ionizing collisions. Such data are available for argon [19], methane [20] and

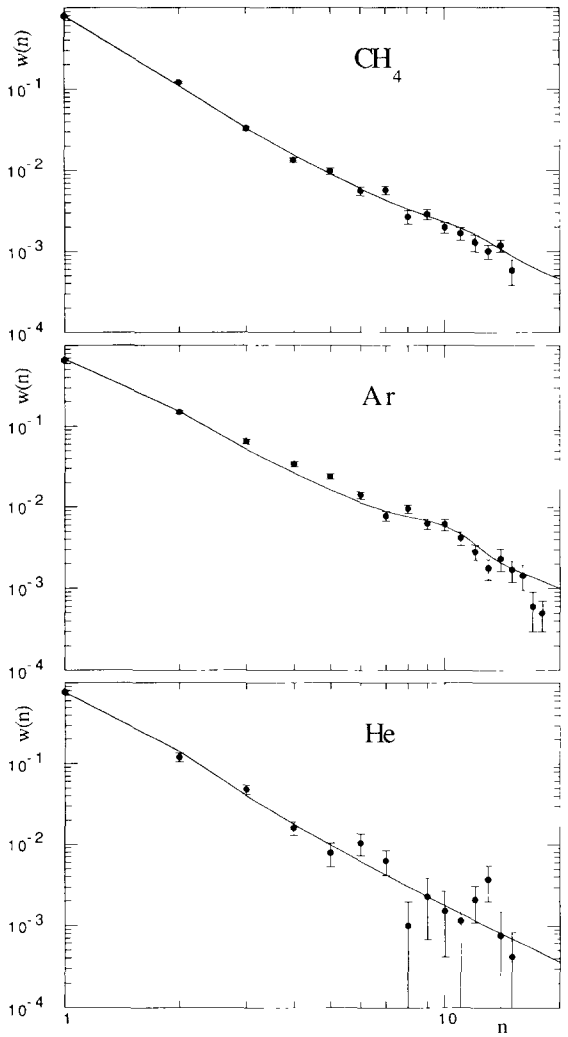

Fig. 13. Comparison of the experimental data for $w(n)$ with the predictions of the model described in section 5.

helium [21]. The kinetic energy T and the differential cross section $d\sigma/dT$ are inserted into eq. (11) replacing the energy transfer E and $d\sigma/dE$. In order to account for the changed energy definitions, the lower and upper limits of the integration are changed to $(n'-1)I_0$ and $n'I_0$, respectively. σ_{tot} is replaced by the integral over the experimental spectrum $d\sigma/dT$. Inner-shell ionization considering the L shell in Ar ($E_L \approx 250$ eV) and the K shell in C ($E_K \approx 270$ eV) is taken into account in the following way: We estimate the probability for energy transfers in excess to E_L (E_K) using eq. (1), normalized to the total primary ionization cross section [15]. For energy transfers exceeding this threshold, we assume that inner and outer-shell ionization take place with a probability proportional to the number of electrons available in those shells. For the total probability of inner-shell ionization we obtain 1% in argon and 0.24% in methane. In these cases, an Auger electron is emitted, in addition to the primary electron carrying the excess of the energy transfer over the binding energy. For use in eq. (11), $d\sigma/dT$ is modified correspondingly. Finally, $w(n)$ is computed using eq. (12). The results are shown in fig. 13. Although the model neglects many of the finer details of atomic physics considered in ref. [4], the agreement with the data is surprisingly good. Also the probability of single electron clusters is well reproduced, see table 4 [#3].

Table 4
Experimental results for the probability $w(1)$ of single electron clusters and predictions of the model described in section 5

	Ar	He	CH_4
Measured [%]	65.6 ± 1.6	76.7 ± 4.2	78.7 ± 1.2
Predicted [%]	67.9	76.1	79.6

We conclude that our measurements give results on the size distribution of ionization clusters which can be used in the design of instruments for particle physics. Our results should also be of interest for some questions of micro-dosimetry. In addition, the data seem to shed new light on the physics of the ionization process.

Acknowledgements

We wish to thank P. Lennert and J. Spitzer for their contributions to this work and J. von Krogh for critical comments concerning this manuscript. The technical help of S. Hennenberger, C. Rummel and R. Rusnyak is greatly acknowledged. This work was supported by the Bundesministerium für Forschung und Technologie, Bonn, Germany.

References

[1] B. Rossi, High-Energy Particles (Prentice Hall, Englewood Cliffs, N.J., 1952)
[2] C.R.T. Wilson, Proc. Roy. Soc. (London) A104 (1923) 192.
[3] W.J. Beekman, Physica 15 (1949) 327.

[#3] The assumption of "electron democracy" made here differs substantially from the model using eq. (13), which gives a strong preference to strongly bound electrons. Our assumption may be justified by the argument that in atomic collisions of fast particles energy and momentum can be balanced between the incident particle and the struck electron, leaving the atomic nucleus as a spectator. In contrast to this, in the absorption of a photon the momentum has to be transferred to the atomic nucleus, hence the sudden increase in $\sigma_\gamma(E)$ whenever strongly bound electrons can be ejected from the atom.

[4] F. Lapique and F. Piuz, Nucl. Instr. and Meth. 175 (1980) 297.
[5] V.A. Chechin et al., Nucl. Instr. and Meth. 98 (1972) 577.
[6] A.H. Walenta, IEEE Trans. Nucl. Sci. NS-26 (1975) 237.
[7] B. Schmidt, Nucl. Instr. and Meth. A252 (1986) 579;
B. Schmidt and S. Polenz, Nucl. Instr. and Meth. A273 (1988) 488.
[8] Similar observations have been reported by H. Genz, Nucl. Instr. and Meth. 112 (1973) 83.
[9] P. v. Walter, IEEE Trans. Nucl. Sci. 35 (1988) 261.
[10] M. Huk, P. Igo-Kemenes and A. Wagner, Nucl. Instr. and Meth. A267 (1988) 107.
[11] F.J. de Heer et al., J. Phys. B12 (1979) 979;
H.F. Winters, J. Chem. Phys. 63 (1975) 3462;
D. Rapp and P. Englander-Golden, J. Chem. Phys. 43 (1965) 1464.
[12] A. Cole, Radiat. Res. 38 (1969) 7; see also ICRU Report 16 (1970/1980), appendix A2.
[13] ICRU Report 31, Int. Com. on Radiation Units and Measurements, Washington, D.C., 1979).
[14] W.P. Jesse and J. Sadaukis, Phys. Rev. 100 (1955) 1755.
[15] F.F. Rieke and W. Prepejchal, Phys. Rev. A6 (1972) 1507.
[16] A. Ore and A. Larsen, Radiat. Res. 21 (1964) 331.
[17] U. Fano, Ann. Rev. Nucl. Sci. 13 (1963) 1.
[18] W.W.M. Allison and J.H. Cobb, Oxford University Nuclear Physics Laboratory Report 13/80.
[19] M.E. Rudd, L.H. Toburen and N. Stolterfold, At. Data Nucl. Data Tables 23 (1979) 405.
[20] D.J. Lynch, L.H. Toburen and W.E. Wilson, J. Chem. Phys 64 (1976) 2616.
[21] M.E. Rudd, L.H. Toburen and N. Stolterfold, At. Data Nucl. Data Tables 18 (1976) 413.